

Influence of defect dynamics on the nanoindentation hardness in NiCoCrFePd high entropy alloy under high dose Xe⁺³ irradiation

Abid Hussain^a, S.A. Khan^a, Sandeep K. Sharma^b, Kathi Sudarshan^b, Saurabh K. Sharma^c, Chetan Singh^d, P.K. Kulriya^{e,*}

^a Materials Science Group, Inter-University Accelerator Centre, New Delhi, 110067, India

^b Radiochemistry Division, Bhabha Atomic Research Centre, Mumbai, 400085, India

^c Mechanical, Aerospace, and Nuclear Engineering, Rensselaer Polytechnic Institute, Troy, NY, 12180, USA

^d Department of Materials Science and Engineering, Indian Institute of Technology, New Delhi, 110067, India

^e School of Physical Sciences, Jawaharlal Nehru University, New Delhi, 110067, India



ARTICLE INFO

Keywords:

High entropy alloy
Irradiation damage
Defect dynamics
Positron annihilation Dopplers broadening spectroscopy
Nanoindentation hardness
TEM

ABSTRACT

We report the role of irradiation-induced defects and microstructure evolution in the wake of 1.05 MeV Xe⁺³ ion irradiation on the structural and mechanical properties of single-phase face-centered cubic (FCC) structured NiCoCrFePd high-entropy alloy (HEA). The defect evolution was investigated using positron annihilation Doppler broadening spectroscopy (PADBS), X-ray diffraction (XRD), high-resolution transmission electron microscopy (HR-TEM), and nanoindentation techniques. Single-phase FCC structured NiCoCrFePd HEA remained structurally stable even upon irradiation to a very high fluence of 9×10^{16} ions/cm². However, an anomalous reduction in the lattice constant, along with micro-strain relaxation and crystallite fragmentation was observed at the initial ion fluence of 1×10^{16} ions/cm², which are recovered upon irradiation at the higher ion fluence due to collapse of small-sized point defects into the large-sized dislocations and simultaneously irradiation-induced recrystallization. Ion fluence-dependent PADBS analysis revealed the formation of mono-vacancies at lower fluence which were saturated by recombination and evolution to large-size defects at successive higher ion fluence that is consistent with electron microscopic investigations. Measurement of mechanical properties showed that the hardness was initially increased by 57% upon irradiation at fluence 1×10^{16} ions/cm² and then it was slightly reduced (~5%) at a higher fluence of 9×10^{16} ions/cm² irradiation due to defect recombination and recrystallization which clearly shows the resistance of this HEA towards hardening. Thus, the present study provides a deeper understanding of the defect dynamics and their relation to the mechanical behavior of NiCoCrFePd HEA, which is important for the development of radiation-resistant alloys for nuclear energy systems.

1. Introduction

During the past few years, multicomponent alloys, also known as high-entropy alloys (HEAs), have drawn huge interest due to their excellent resistance to irradiation-induced swelling, hardening, voids formation and bubble formation, which leads to improvement in their structural and mechanical stability on the exposure to severe radiation [1] [-] [3]. These properties are attributed to their intrinsic nature of chemical complexity, large lattice distortion and short-range ordering [4,5]. Several studies show that the presence of different types of atoms not only increases the chemical complexity but also produces lattice distortion and short-range ordering, because of the different size atoms

occupying random lattice positions in the same crystal structure [6,7]. The presence of a high degree of lattice distortion and short-range ordering in HEAs compared to conventional alloys and pure metals alters the generation mechanism of irradiation-induced defects, defects recombination, and their migrations. Zhang et al. explained that irradiation-induced embrittlement, hardening, and cracking are produced due to the movement of vacancies and the formation of voids and dislocation [8]. One of the ways to avoid such failure is to hinder the movement of vacancies inside the matrix, which also enhances the probability of recombination with an interstitial. The electron microscopic studies showed that smaller-sized defects are produced in HEAs as compared with the conventional alloys, because of the hindrance in

* Corresponding author.

E-mail address: pkkulriya@mail.jnu.ac.in (P.K. Kulriya).

motion of vacancies in HEAs due to the incorporation of different size elements producing lattice distortion [9]. In addition, the HEAs have the inherent property of containing different size elements which can be utilized as a tool to modulate the defect kinematics and to make these radiation tolerant materials [10]. Among various single-phase FCC HEAs, the Pd-based HEAs, namely NiCoCrFePd, showed the presence of significant lattice distortion with atomic scale inhomogeneity due to the large lattice mismatching generated by the incorporation of Pd, which makes them a suitable candidate for the study of generation and migration of vacancies [5,11]. Moreover, the Pd addition has other significant effects e.g. high yield strength (410 MPa for NiCoCrFePd vs. 166 MPa for NiCoCrFe) [5,12], reduced thermal conductivity and thermal diffusivity, high electrical resistivity etc. [13,14]. These alloys also showed an enhanced radiation tolerance which is directly related to lattice distortion and slowdown of dislocation motion in the complex alloy [15]. Observation of smaller size dislocation loops in NiCoCrFePd alloy (4.7 ± 1 nm) as compared to NiCoCrFeMn (15.9 ± 1 nm) on 3.0 MeV Ni⁺ ion irradiation at 693 K confirmed a dramatic effect on the size and density of the dislocation loops as well as the strong pinning effect of Pd [16]. Although, the quantification of small size defects using TEM is difficult due to the limited traceability of small vacancy type of defects generated by ions thus, positron annihilation spectroscopy (PAS) is used to detect such small size defects.

PAS is a unique tool for investigating various defects ranging from vacancies to dislocation loops because of its high sensitivity towards open-volume defects [17,18]. The variable energy of the positron makes it possible for depth-dependent studies in irradiated alloys. The generation of mono-vacancies at the lower dose and stacking fault tetragonal (SFT) at the high dose is reported in the NiCoCrFe under 1.5 MeV Ni⁺ [19] using PAS. Similarly, the formation of the He-vacancy complex which act as a deep trap for positron in NiCoCrFe is reported on He⁺ ion irradiation [20]. The positron annihilation lifetime measurement studies of quinary HEA for example NiCoCrFeMn and AlCoCrFeNi showed the absence of any open volume in the bulk except on the surface due to surface defects [21,22]. However, the dynamics of the defects produced under ion irradiation and their correlation with the mechanical performance of such alloys are missing in literature. Only a few studies have been performed on binary, quaternary medium entropy alloy and non equi-atomic HEA [4,23]. For example, PAS and TEM studies on Zr-Nb binary alloys showed the formation of dislocation even at a lower dose (2.5 dpa Xe-ions) and found them susceptible to severe irradiation damage at high dpa. In contrast, no literature is available to track down the defect dynamics with its effects on mechanical properties for a quinary HEAs, even though their resistance against irradiation effects was found many fold higher than other alloys [7,9,24]. The evidence of smaller dislocation loop size in Pd incorporated NiCoCrFe compared to NiCoCrFeMn [25,26] clearly shows its high resistance towards irradiation.

Thus, the present study probes the types of the defect generated by using 1.05 MeV Xe⁺³ ion irradiation and its effect on the hardness of the NiCoCrFePd by employing the PADBS, TEM and nanoindentation techniques. Further, the influence of ion fluence or dose on the evolution of these defects and its effect on the mechanical properties is also studied.

2. Experimental details

High purity grade Nickel, Cobalt, Chromium, Iron and Palladium metal basis from Alpha Aesar and Sigma Aldrich were used as primary precursors for the synthesis of bulk HEA namely, NiCoCrFePd using a conventional Arc-Melting technique. Details of the synthesis can be found elsewhere [13]. The homogenization of the as melted button was carried out at 1200 °C temperature for 24 h in a vacuum of the order 10^{-2} mbar. The well-annealed button was then cold rolled to reduce the thickness by 90 (%) of the initial thickness. These cold-rolled samples of final thickness ~2 mm were further annealed at 800 °C for 1 h in an ultra-high vacuum to remove the defects due to rolling. Finally, six

specimens of size (7 mm × 10 mm × 3 mm) were cut using a low-speed diamond wheel saw and further mechanically polished using a SiC abrasive paper of 1500 grit and a diamond lapping compound to achieve a mirror-like surface finish. Two of the mechanically polished samples were further thinned down to ~80 µm using a polishing machine and 3 mm disk was fabricated with help of disc puncher. These disks were then thinned down to electron transparency using a twin jet electro-polishing machine (TenuPol-5) with the electrolyte mixture of 90 mL ethanol and 10 mL perchloric acid at 30 mA and temperature -25 °C. One of these specimens meant for TEM characterization was mounted on a stainless-steel TEM sample holder along with three mechanically polished specimens were fixed on the copper ladder with a carbon tape for 1.05 MeV Xe⁺³ ion irradiation at a high flux of 3.12×10^{13} ions/(sec-cm²) using the low energy ion beam facility (LEIBF) available at Inter-University Accelerator Centre, New Delhi. A raster-scanned Xe beam was used to irradiate the samples uniformly at room temperature. The fluence was varied from 1×10^{16} ions/cm² to 9×10^{16} ions/cm² by keeping the target sample at room temperature. The TEM specimen was directly exposed to the beam at the highest fluence 9×10^{16} ions/cm² by holding the disk in a stainless steel-holder and attaching it to the copper ladder. The theoretical simulation of the damage profile is shown in Fig. 1 (in displacement per atom or dpa unit), obtained using the SRIM [27] (Stopping and Range of Ions in Matter) software in the Kinchin-Pease option with displacement energy for all atoms taken as 40 eV, as suggested to use for simulations of ion irradiation damage in dpa calculation [28].

It is observed that the maximum damage goes up to 392.8 dpa at 80 nm depth for the highest fluence 9×10^{16} ions/cm² with a maximum range of damage up to 250 nm in depth.

Structural and phase analysis of the pristine and irradiated specimens was carried out using an X-ray diffractometer (PANalytical make; X'Pert3 model) with a Cu K_α X-rays source operating at a voltage of 45 kV and current of 40 mA. The diffraction data was collected at a glancing incidence angle of 1° by 2θ scanning from 40° to 100° with a scan speed 1°/min in a 0.02° step size, using a scintillation detector. The structure along with the composition measurements was carried out by using a field emission scanning electron microscopy (MIRA-II LMH, TESCAN) equipped with an energy dispersive X-ray detector (INCA) to verify the equi-atomic ratio of each element in the alloy. A Transmission Electron Microscope (HR-TEM)-JEOL 2100F operating at 200 keV was used for microstructural characterization of the pristine and irradiated TEM-

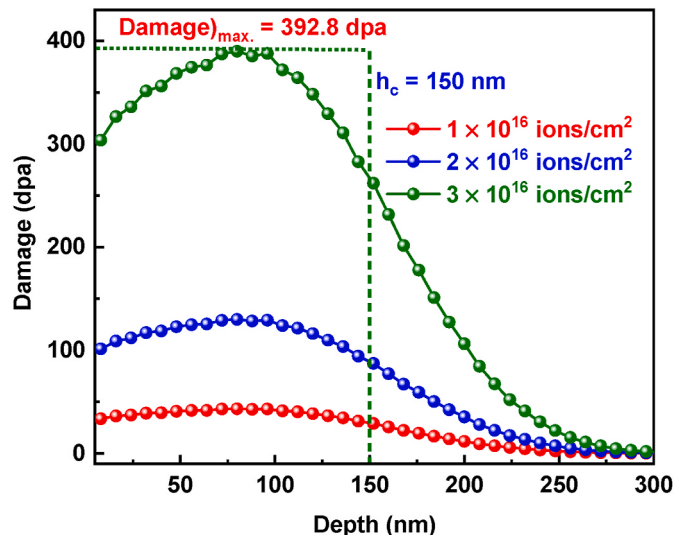


Fig. 1. SRIM predicted damages (dpa) with depth variation for ion fluence 1×10^{16} , 3×10^{16} and 9×10^{16} ions/cm² marked with maximum damage of 392.8 dpa corresponding to highest fluence and experimentally determined critical depth (h_c) = 150 nm.

specimen.

The depth-dependent Doppler broadening measurements of the pristine and the irradiated samples were carried out using an HPGE detector with an energy resolution of 2.0 keV at 1332 keV of ^{60}Co , coupled to a slow positron accelerator available at the Bhabha Atomic Research Centre (BARC), Mumbai [29]. Positrons emitted from a ^{22}Na source (activity ~ 20 mCi) were moderated using a W (001) film. The thermalized positrons emitted from the moderator are transported to the sample chamber through a solenoid in the magnetic field. The uniformity of the magnetic field was maintained in the sample chamber using Helmholtz coils. The monoenergetic positrons were accelerated by applying the requisite negative voltage to the sample. The annihilation gamma photo peaks (total counts $\sim 2 \times 10^6$ counts) were acquired at different positron implantation energy. The annihilation peak was characterized by line shape parameters viz. S-parameters and W-parameter. S-parameter is defined as the ratio of counts in the central region (511 ± 0.77 keV) to the total counts in the annihilation photo peak. W-parameter is defined as the contribution in the wing region and calculated as counts under $2.30 \text{ keV} \leq |\text{E}_\gamma - 511| \leq 5.76 \text{ keV}$ region to the total area of the photo peak. The variable energy positron fit (VEPFIT) computer program has been used to fit the experimental S-E and W-E profiles to evaluate the characteristic S and W parameters and diffusion length of positrons in the damaged region [30]. Finally, the nanoindentation hardness was measured using a Universal Nanomechanical tester (ASMEC, Germany). The testing was performed using a Berkovich indenter with a tip radius of 153 nm. The quasi-continuous stiffness measurement (QCSM) mode was used with a maximum load of 40 mN with an intender depth going up to 700 nm. During the measurement, at least 5 indents were made normal to the sample surface at distinct places, with a loading rate of 1 mN/s.

3. Experimental results

3.1. XRD investigation

Xe-ion irradiation in materials leads to high damage production due to the high nuclear energy loss S_n (12 keV/nm) owing to its high Z value. The irradiation of Xe^{+3} ions in NiCoCrFePd HEA is expected to produce

more point defects due to the exceptional local lattice distortion present in the alloy compared to the parent NiCoCrFe. Fig. 2(a) shows the X-ray diffraction patterns of pristine and ion-irradiated NiCoCrFePd HEA with fluence 1×10^{16} , 3×10^{16} and 9×10^{16} ions/cm 2 . The diffraction pattern for the pristine sample shows that the prepared lattice structure stabilizes in a single-phase FCC structure with lattice parameter 3.666 Å, similar to the reported value of 3.67 Å in the literature [13,26]. It can be clearly seen from Fig. 2(a), that the peaks indexed as (111), (200), (220), and (311) correspond to the FCC structure of the pristine alloy with no other peak, signifying the robust structural stability even at the peak damage of 392.8 dpa. The concentration for the alloy obtained using EDX appears in a ratio of 19.28, 20.38, 19.45, 19.24, and 21.65 atomic % corresponding to elements Cr, Fe, Co, Ni, and Pd respectively, which is approximately equal to the nominal equi-atomic composition [see S1 in the supplementary]. With the exposure to ion irradiation at different ion fluences, the peaks show a variation in the intensity, peak positions, and FWHM parameters [Fig. 2(a)]. On irradiation at the lowest ion fluence (1×10^{16} ions/cm 2), peak shift is observed towards a higher 2θ value accompanied by an increment in FWHM. But on subsequent irradiation at higher ion fluences, the observed shifting in 2θ reverse and the FWHM starts reducing as shown in zoomed [111] peak in Fig. 2(b). In order to estimate the crystallite size and microstrain, the Williamson Hall (W-H) analysis was carried out using the equation [31].

$$\beta \cos(\theta) = k\lambda/D + 4\epsilon \sin(\theta) \quad (1)$$

Here, $k = 0.9$ for cubic crystals, β is the full width at half maximum (FWHM), D is crystallite size, ϵ is microstrain, λ and θ have the usual meanings. In the W-H plot, [see S2 in the supplementary] β was obtained by fitting the individual peak using a pseudo-Voigt function. The calculated value of the crystallite size and the microstrain of the pristine, as well as the irradiated samples from the W-H plot, are tabulated in Table 1. The variation in the microstrain and the crystallite size with the ion fluence is also shown in Figs. 2(c) and Fig. 8(b). The crystallite size and lattice microstrain (%) were found to be $\sim 12.67 \pm 0.30$ nm and 0.55 ± 0.02 for the pristine sample, which reduce to a value of $\sim 5.92 \pm 0.24$ nm and 0.33 ± 0.16 , respectively upon irradiation to a fluence of 1×10^{16} ion/cm 2 . Due to the abrupt reduction in the crystallite size and

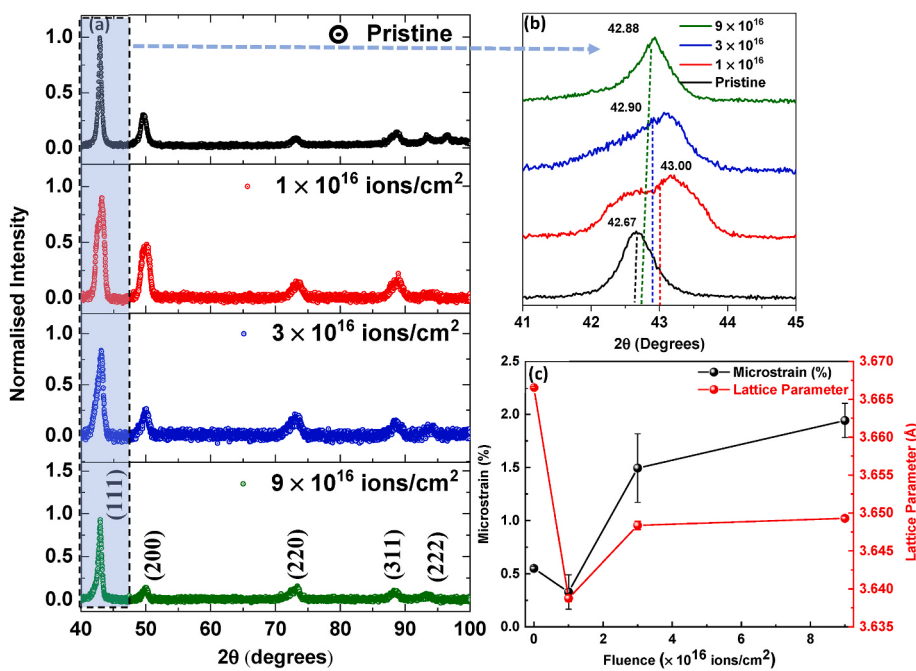


Fig. 2. XRD pattern of pristine NiCoCrFePd HEA with single phase FCC structure and ion irradiated with fluence 1×10^{16} , 3×10^{16} and 9×10^{16} ions/cm 2 (b) zoomed part of [111] peak showing the peak shifting, and (C) microstrain (%) and lattice parameter variation with ion fluence.

Table 1

Fitted parameters from XRD fittings corresponding to different fluence.

Fluence (ions/cm ²)	Crystallite size (D) (nm)	Macrostrain (ε) (%)	Peak damage/dose (dpa)
Pristine	12.67 ± 0.30	0.55 ± 0.02	0
1 × 10 ¹⁶	5.92 ± 0.24	0.33 ± 0.16	42
3 × 10 ¹⁶	6.29 ± 0.20	1.50 ± 0.32	130
9 × 10 ¹⁶	10.05 ± 0.40	1.94 ± 0.16	392

the lattice strain, the lattice relaxation from 3.666 Å to 3.639 Å is observed as shown in Fig. 2(c).

Further, when ion fluence is increased to 3 × 10¹⁶ ions/cm², a reverse trend in the variation of crystallite size and the lattice strain is observed [Table 1], probably associated with the larger size defects created by ions at higher ion fluence, similar to the observation of stacking fault tetragonal (SFT) along with vacancies at higher ion fluence as evident from the positron annihilation Dopplers broadening spectroscopic study by Abhyu et al. [19]. On the subsequent increase in the ion fluence to 9 × 10¹⁶ ions/cm² a further, increase in crystallite size and lattice microstrain (%) to 10.05 ± 0.40 nm and 1.94 ± 0.16 was observed.

3.2. PAS investigation

Positron annihilation spectroscopy (PAS) is a unique tool to identify the nature, size and concentration of defects generated by ion irradiation [32] [–] [34]. Moreover, PAS is a very sensitive technique to probe open volume defects in HEAs which act as deep traps for positron [21,22,35]. It is reported that the dislocation and the vacancy clusters created during the irradiation serve as deep positron traps in alloys and metals [18,36,37]. Fig. 3(a) shows the depth-dependent S-E profiles of the pristine NiCoCrFePd HEA and irradiated specimens with 1.05 MeV Xe⁺³ ion at various ion fluence ranging from 1 × 10¹⁶ ions/cm² to 9 × 10¹⁶ ions/cm². The solid lines drawn through the data points show the fitting of S-E profiles using VEPFIT. According to VEPFIT, a sample can be considered as multi-layered depending on the depth-dependent defect distributions of open-volume defects. A sample having different types of defect characteristics at different depths can be distinguished by different values of the corresponding line shape parameter. Positron implantation profile follows a Makhovian profile in materials which becomes broader with the increase in the implantation energy. According to this profile, the mean implantation depth $\langle z \rangle$, nm of the positron is calculated using the following expression:

$$\langle z \rangle \geq 40E^{1.6}/\rho \quad (2)$$

where E (keV) is the implantation energy and ρ is the density (g/cc) of

the material [38]. The mean implantation depth calculated using this expression is shown on the top axis of Fig. 3(a). As a result of the broadening of positron implantation profile with the implantation energy, experimental line shape parameters have contributions from different regions of the sample having different defect characteristics. In addition, positrons also undergo diffusion on implantation in the material making elastic/inelastic collisions with constituent elements. According to VEPFIT, considering the broadening of implantation profile and diffusion of positron in the material, the S-parameter at particular implantation energy (E) in a sample consisting of (i) number of layers of different defect characteristics can be expressed as:

$$S(E) = S_{surf}f_{surf} + \sum_{i=1}^k S_i f_i \quad (3)$$

where S_{surf} and S_i are S-parameter values corresponding to the surface and i th layer of the sample, respectively. Parameters f_{surf} and f_i represent the fraction of positrons annihilating at the surface and in the i th layer of the sample [30].

S-E profiles of the unirradiated sample follow a typical trend of metallic specimens [37]. S-parameter values reduced with the increase in implantation energy and reached a constant value beyond ~7.5 keV implantation energy. Such a decrease in S-parameter value with the increase in implantation depth is attributed to the back diffusion of positrons. These positrons reach the surface where they annihilate through a positronium-like state having a narrower momentum distribution (higher S-parameter). On implantation of positrons deeper in the sample, the fraction of positrons reaching the surface through back diffusion decreases leading to a reduction in the S-parameter value. Depending on the positron diffusion length in the sample, the S-parameter value reaches a constant value at a particular positron implantation energy.

In order to carry out the fitting of the S-E profile of unirradiated sample using VEPFIT, two layers were considered with one being a very narrow surface layer (~20 nm) with a very short diffusion length of ~9 nm. Such a defected surface layer has been observed in various studies and it is attributed to the surface defects like SFT present in the subsurface region. The diffusion length in the second layer i.e., the bulk layer was evaluated to be ~73.8 ± 5.7 nm which is shorter than the diffusion length measured in bulk defect-free metals ~(100–150 nm) [4]. The shorter value of diffusion length confirms the presence of open-volume vacancy defects in the sample which act as traps for positrons leading to a reduction in their diffusion. On 1.05 MeV Xe⁺³ ion irradiation, the S-E profile of the samples is distinctly modified and the S-parameter increases appreciably in positron implantation energy range ~(2.5–20) keV with a hump peaking in energy range ~(5–12)

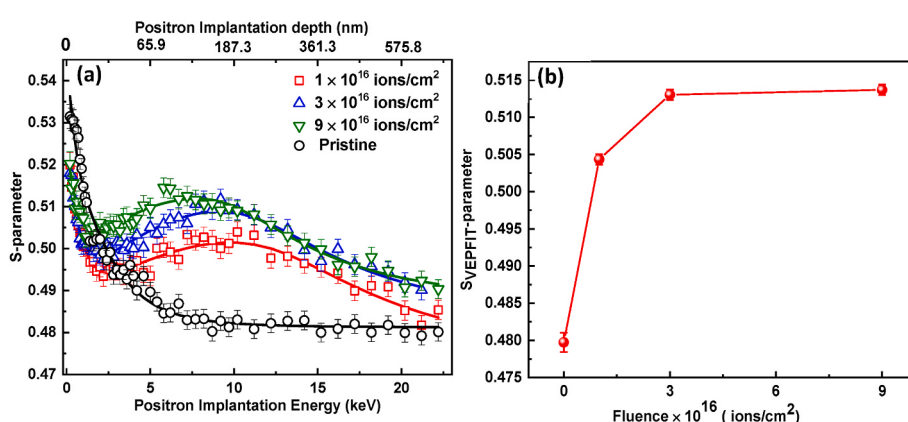


Fig. 3. (a) S-E profiles of pristine and irradiated NiCoCrFePd HEA samples with fluence 1 × 10¹⁶, 3 × 10¹⁶ and 9 × 10¹⁶ ions/cm². The solid lines through the data points show the fitting of the S-E profiles using VEPFIT, and (b) S-parameter evaluated using VEPFIT corresponding to the second layer (damaged region) of the HEA samples irradiated with varying fluence of Xe-ions.

keV. This shows that the electron-positron momentum distribution is narrower in the modified region, which clearly signals the formation of vacancy type of defects. The S-E profiles of the irradiated samples shown in Fig. 3(a) are qualitatively similar to the SRIM (dpa) profiles as shown in Fig. 1. The S-E profiles of the irradiated samples have been fitted using VEPFIT considering a three-layer model since considering single or two layers did not reproduce the experimental S-E profiles. The first 20 nm thick layer at the surface is considered to take care of the surface artifact such as SFT and sputtering, etc and does not carry any significant information regarding the open volume defects created due to ion irradiation. The third layer is considered as bulk of the sample which remains undamaged due to the limited range of ion implantation. The evaluated diffusion length values corresponding to the second layer which represents the damaged region of the samples are 67.0 ± 7.8 , 62.2 ± 5.6 , and 31.8 ± 4.8 nm for irradiation fluence of 1×10^{16} , 3×10^{16} and 9×10^{16} ions/cm 2 , respectively as given in Table 2. The diffusion length value decreases with the increase in the implantation dose confirming the increase in open-volume defects in the samples with the ion irradiation fluence. Also, the sharp transition of the S-parameter from the surface value to the bulk value is attributed to the shortening of the positron diffusion length with the increase of density of vacancies at higher ion fluence. It is interesting to note that the boundary layer of the second layer given in Table 2 is higher than the ion range predicted by SRIM, which is attributed to the cascade effects in the lattice and channelling as well as straggling, as it is reasonable that in SRIM calculation of defect does not consider the diffusion of defects, the interaction of defects and channeling. The boundary layer thickness corresponding to the second layer of Xe $^{+3}$ ion irradiated samples is observed to decrease continuously with the increase in the Xe $^{+3}$ fluence. The observed decrease in the boundary layer thickness indicates that open volume defects are occupied by the interstitials or implanted Xe-ions. Fig. 3(b) shows the variation of the S-parameter evaluated using VEPFIT corresponding to the damaged region of the samples. It is observed that the S-parameter value corresponding to the damaged region does not increase linearly with total fluence. It confirms that the open-volume density does not increase continuously with the ion fluence and reaches to a saturation. The W-E profile shown in Fig. 4 also behaves similar to the S-E profile, with the ion fluence, initially the W parameter decreases in the range (2.5–20) keV and reaches to a minimum value at 7.5 keV positron energy. To evaluate the W-parameter corresponding to the damaged region of the samples, W-E profiles have been fitted using VEPFIT following the same methodology. In order to reduce the number of fitting parameters, diffusion length and boundary layer values evaluated from S-E fittings have been used as fixed parameters for W-E fittings. The evaluated W-parameters corresponding to the damaged region are also given in Table 2. In order to further distinguish the type of defects in the sample, the S-W correlation has been plotted. S-W correlation of experimental data points of pristine sample follows a straight trend line as shown in Fig. 5. It confirms that the pristine sample has a uniform depth distribution of defects. The S-W data trend line corresponding to the damaged region of the irradiated sample with the lowest fluence (1×10^{16} ions/cm 2) falls nearby the trend line indicating that type of defects are the same as in the pristine sample. On the other hand, S-W data points corresponding to higher

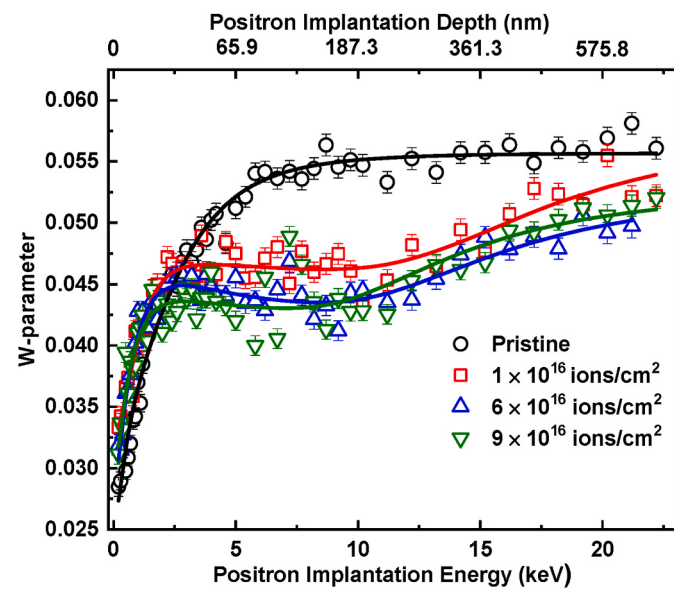


Fig. 4. W-E profiles of pristine and irradiated NiCoCrFePd HEA samples with fluence 1×10^{16} , 3×10^{16} and 9×10^{16} ions/cm 2 . The solid lines through the data points show the fitting of the W-E profiles using VEPFIT.

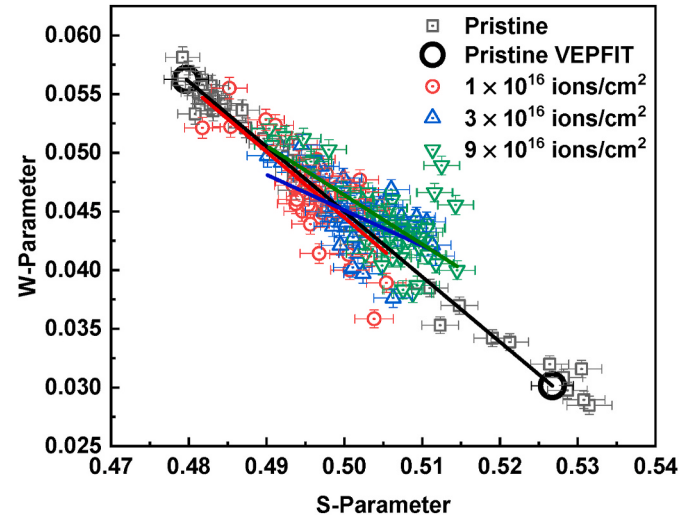


Fig. 5. S-W correlation of pristine sample along with the data points corresponding to surface and bulk region evaluated using VEPFIT. The S-W data points corresponding to the damaged region of irradiated samples are also shown. The solid lines are an eye guide to show the linear correlation.

fluence sample do not follow the trend line and indicate that in addition to an increase in the density of defects, different types of defects are also generated which can be attributed to large size dislocation defects as observed in the (HR-TEM) explained in the next subsequent section.

3.3. TEM characterization

In order to probe the type of defects produced at the highest ion fluence, the HR-TEM analysis was carried out for the pristine and sample irradiated with Xe $^{+3}$ at a fluence 9×10^{16} ions/cm 2 as shown in Fig. 6 (a-f). It shows that the structure of NiCoCrFePd HEA remains intact and no voids formation takes place at the peak dose of 392.8 dpa irradiated at room temperature. In contrary, swelling and void formation with a void density of $(1.6 \pm 0.12) \times 10^{20}$ m $^{-3}$ are reported for 3 MeV Ni $^{+2}$ ion irradiation at lower dose (38 ± 5 dpa) and at a high temperature of 853

Table 2

Line shape parameters (S and W) and positron diffusion length, D_L(nm) corresponding to bulk of unirradiated sample and damaged region of the Xe irradiated samples evaluated using VEPFIT. The boundary layer, B_L (nm) of the damaged region is also given.

Fluence (ions/cm 2)	S-parameter $\leq \pm 0.0020$	W-parameter $\leq \pm 0.0002$	D _L (nm) $\leq \pm 5.0$	B _L (nm) $\leq \pm 15.0$
Pristine	0.4797	0.0563	73.8	Infinite
1×10^{16}	0.5043	0.0457	67.0	518
3×10^{16}	0.5130	0.0427	62.3	428
9×10^{16}	0.5137	0.0427	31.8	335

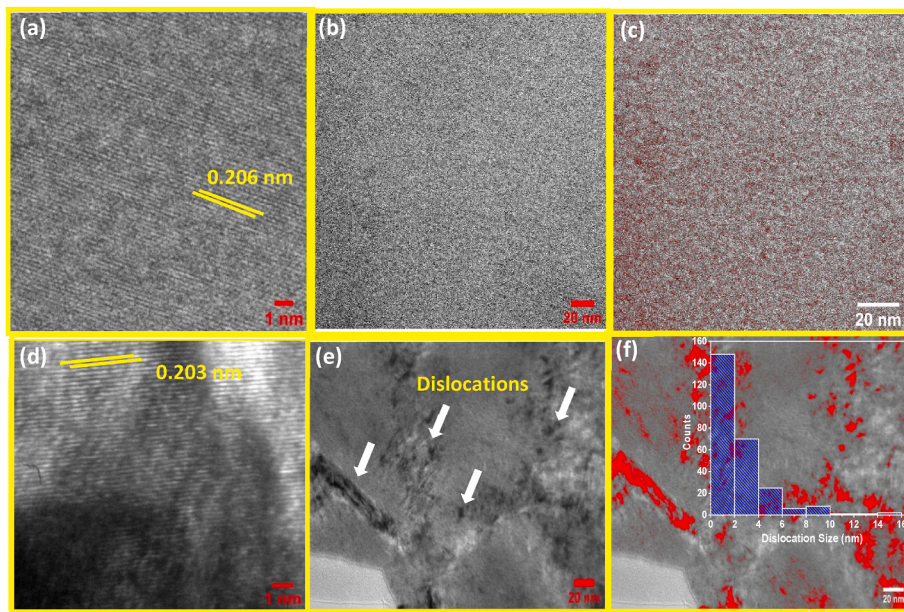


Fig. 6. Bright field TEM micrograph image of NiCoCrFePd HEA. (a–c) shows images of pristine sample with (a) the lattice spacing of pristine sample, (b) microstructure at higher magnification, (c) image thresholding with red colour exhibits no damage region, and (d–f) image of ion irradiated sample with (d) lattice spacing of sample irradiated with ion fluence 9×10^{16} ions/cm 2 (e) microstructure with dislocations by white arrows, and (f) image thresholding with red colour to highlight the damaged region having dislocations, and inset histogram depict the dislocation distribution formed after irradiated at fluence 9×10^{16} ions/cm 2 Xe $^{+3}$ ions. (For interpretation of the references to colour in this figure legend, the reader is referred to the Web version of this article.)

K which clearly exhibits the effect of temperature on the void swelling [16]. It may be noted that significant number of the irradiation induced dislocation were produced which are marked by white arrows in Fig. 6(e). The observed value of the dislocation loops was in the range of (2 nm–16 nm) with mostly small size dislocation as shown in histogram Fig. 6(f) inset. The dislocation density calculated using the formula $\rho = N/A$, where N , is the total numbers of dislocation in area A (289.25 nm $\times 188.83$ nm) is found to be 4.815×10^{15} m $^{-2}$. The observation of relatively higher dislocation density in the room temperature irradiated NiCoCrFePd HEA as compared to 3 MeV Ni $^{+2}$ ion irradiation ($\sim 10^{14}$ m $^{-2}$ at 853 K) is associated with lesser defect recombination at room temperature irradiation as compared to high temperature irradiation [16]. In addition, the value of interplanar spacing for the pristine comes out to be 0.206 nm which gets shrunk to 0.203 nm on irradiation to a fluence 9×10^{16} ions/cm 2 in consistent with XRD analysis Fig. 2(c). The estimated value of lattice constant from the interplanar spacing was found 3.567 Å and 3.516 Å corresponding to the pristine and irradiated sample with ion fluence 9×10^{16} ions/cm 2 as shown in Fig. 6(a) and (b). The anomalous lattice contraction (~1.4%) is observed because of inherent existence of extreme lattice distortion due to the presence large-size Pd in the pristine sample which is an observation contrary to the conventional alloy systems under irradiation [39]. Such anomalous behavior is also reported in Ti $_2$ ZrHfV $_{0.5}$ Mo $_{0.2}$ HEA with a lattice contraction of 0.676% [4].

3.4. Nanoindentation measurement

Nanoindentation measurements were carried out to investigate the effect of ion irradiation on the nanoindentation hardness of the NiCoCrFePd HEA. Fig. 7(a) shows the typical behavior of hardness versus depth profile for the pristine and irradiated NiCoCrFePd HEA at various ion fluence. The usual decrease in the hardness with the depth for the pristine is attributed to the indentation size effect (ISE) [40]. With ion irradiation to the lowest ion fluence of 1×10^{16} ions/cm 2 , the magnitude of the hardness is increased but it follows a similar trend as the pristine sample. Such an increase in the hardness to 4.779 GPa from 1.948 GPa at initial ion fluence of 2.5×10^{17} He $^+$ ion/cm 2 irradiation is also reported for CoCrFeCuNi HEA and attributed to the restriction in the atomic motion due to dislocation being produced during the ion irradiation [8,41]. Similarly, the irradiation of Inconel 617 using Xe $^{+20}$ at varying doses till 10 dpa found an increase in hardness to 5.33 ± 0.29 GPa from pristine value of 2.95 ± 0.04 GPa [42]. When the ion fluence is subsequently increased a small reduction in the hardness to 4.12 ± 0.07 GPa and 3.95 ± 0.08 GPa was observed which is attributed to the defect recombination and recrystallizations [43]. However, a slight increase in the hardness up to a critical depth is also observed with the increases in depth for all the values of the fluence. The degree of increment in hardness can be better visualized from the variation in the normalized hardness ($H_{\text{irr}}/H_{\text{Unirr}}$) with depth as shown in Fig. 7(b). It can be clearly

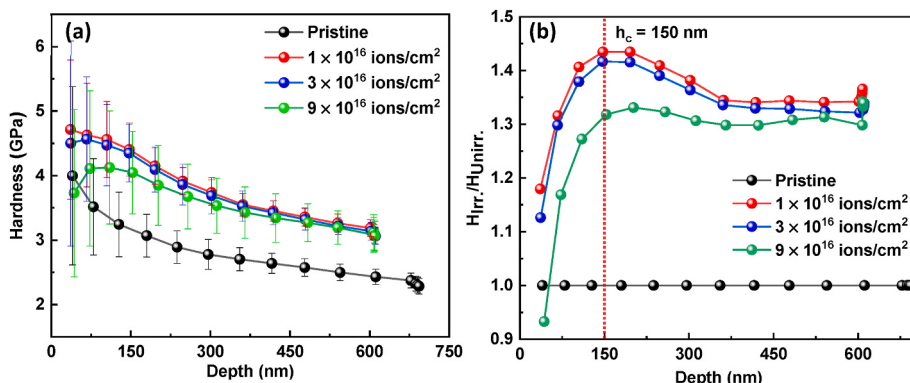


Fig. 7. Variation in the (a) hardness, and (b) ratio of $H_{\text{irr}}/H_{\text{Unirr}}$, with depth for pristine and irradiated NiCoCrFePd HEA with fluence 1×10^{16} , 3×10^{16} and 9×10^{16} ions/cm 2 .

seen that the normalized hardness ($H_{\text{irr}}/H_{\text{Unirr}}$) in the shallower region increases up to a critical depth $h_c \sim 150$ nm then reduced in the deep shallow region which is similar to the trend as reported for other HEAs [8,36]. These variations arise because of the indentation hemisphere zone and the influence of which reaches (4–10) times the indentation depth. If the thickness of the hardened layer is higher than the indentation depth, the ratio increases otherwise it decreases due to the soft substrate effect which comes into play [44].

Nix and Gao model based on the geometrically necessary dislocation is used to address the ISE. This model predicts the true hardness by using the equation as follows:

$$\frac{H}{H_0} = \sqrt{\left(1 + \frac{h^*}{h}\right)} \quad (4)$$

where, H_0 is the true value of hardness i.e., the hardness in the modified region, H is the hardness at a depth of h and h^* is the characteristic length that depends on the indenter tip geometry and on the type of material. Fig. 8(a) shows H^2 vs. $1/d$ plots, marked with the critical depth (h_c) and Fig. 8(b) shows variation of crystallite size and hardness with ion fluence for pristine and irradiated NiCoCrFePd HEA. The linear fittings corresponding to different curves of H^2 vs $1/d$ are also shown in Fig. 8(a). The linear fitting of the pristine sample is carried out in the depth range of 80 nm–180 nm while fitting for the irradiated sample is done from 66 nm to 150 nm depth, considering the information that the modified region due to ion irradiation lies within the SRIM predicted dpa profile region shown in Fig. 1. The fitting parameters H_0 and h^* calculated using the least square fitting of the experimental hardness values are tabulated in Table 3. The shallower region (<66 nm) from the surface is neglected to avoid the contribution from the surface defects like dislocation and sputtering. Also, the irradiated samples exhibit binlinearity that corresponds to the modified region due to ion irradiation and the unmodified region with a shoulder peaking at the critical depth $h_c \sim 150$ nm for all the irradiated samples [Fig. 8(a)]. In addition, increase in the hardness of the irradiated region (H_0) at initial ion fluence of 1×10^{16} ions/cm 2 can be directly correlated with reduction in the crystallite size and follows opposite trend on the irradiation at the subsequent ion fluence where the hardness decreases with increase in the crystallite size at the ion fluences to 3×10^{16} ions/cm 2 and 9×10^{16} ions/cm 2 [Fig. 8(b)].

4. Discussion

The experimental results of the structural and mechanical properties probed using PADBS, XRD, HR-TEM and nanoindentation techniques suggest that excessive defects are produced due to ion irradiation which affect the mechanical properties of NiCoCrFePd HEA. The vacancies and interstitials are generated at the initial ion fluence (1×10^{16} ions/cm 2) acts as deep positron traps as evident from sharp increase in S-value

which is saturated at higher fluence as shown in Fig. 9(b). In addition, observation of the similar linear S-W correlation line for pristine and HEA irradiated to a fluence 1×10^{16} ions/cm 2 confirmed that the nature of defects produced at 1×10^{16} ions/cm 2 is similar to that present in pristine [Fig. 3(b)]. These results are evidence of production of vacancy type of defects which diffuses towards the surface with increase in the Xe ion fluence. Thus, increase in the nanoindentation hardness (H_0) of the irradiated sample (4.16 ± 0.11 GPa) from the pristine value (2.64 ± 0.03 GPa) owing to abrupt increase in vacancies at the initial ion fluence [Fig. 9(b)] and decrease in the crystallite size [Fig. 8(b)]. These results clearly indicates that the hardening behavior due to ion irradiation at the initial ion fluence of 1×10^{16} ions/cm 2 are induced by vacancies. Further the vacancy concentration can be connected to the positron diffusion length considering only a vacancy type of defect concentration (C_D) in the alloy by the equation:

$$C_D = \frac{1}{\mu \tau_b} \left(\frac{L_b^2}{L_D^2} - 1 \right) \quad (5)$$

Where μ is the trapping coefficient, τ_b is the bulk lifetime, L_b is the effective diffusion length in the non-defected region, and L_D is the diffusion length in the damaged region. For the estimation of C_D , a vacancy type of defect with the value of $\mu = 10^{14}$ s $^{-1}$ is assumed and the average bulk lifetime ($\tau_b = 112$ ps) for a vacancy type of defect is taken as reported for defect free NiCoCrFeMn [21,45] due to non-availability of the value for the NiCoCrFePd HEA and the diffusion length L_b for a defect-free state is taken as 160 nm [46].

Using the diffusion length values from Table 2, the calculated values of the C_D are 2.69×10^{19} , 3.41×10^{19} , 4.08×10^{19} and 1.76×10^{20} cm $^{-3}$ corresponding to the pristine, and irradiated with fluence 1×10^{16} , 3×10^{16} and 9×10^{16} ions/cm 2 samples, respectively. It is found that the vacancy concentration increase with ion fluence as shown in Fig. 9(a), which contradicts the results obtained from the saturating S-value calculated using VEPFIT [Fig. 9(b)]. Thus, appreciable vacancies at higher fluence collapse owing to their recombination due to migrations of interstitials. Because of the high mobility of interstitial at room temperature and also due to the significant strain imparted by the incoming Xe-ions in the HEA matrix as evidenced from Fig. 2(c), it is also quite possible that the defect motion may be linked to the Xe-ions concentration as also observed in Aluminium and Titanium implanted with Xe-ions at higher ion fluence [37,47]. The induced stress modulated the interstitials to migrate to low stress regions and thus generates dislocations loops [48,49]. In addition, the short diffusion length [Table 2] at high fluence extracted from the S-E plot supports such migration of defects towards low stress surface region. On the subsequent increase in the ion fluence to 3×10^{16} ions/cm 2 and 9×10^{16} ions/cm 2 , the formation of dislocation is observed because of point defect and cluster migration as indicated by the deviation of straight line from the pristine line in the S-W correlation [Fig. 5]. The dislocation

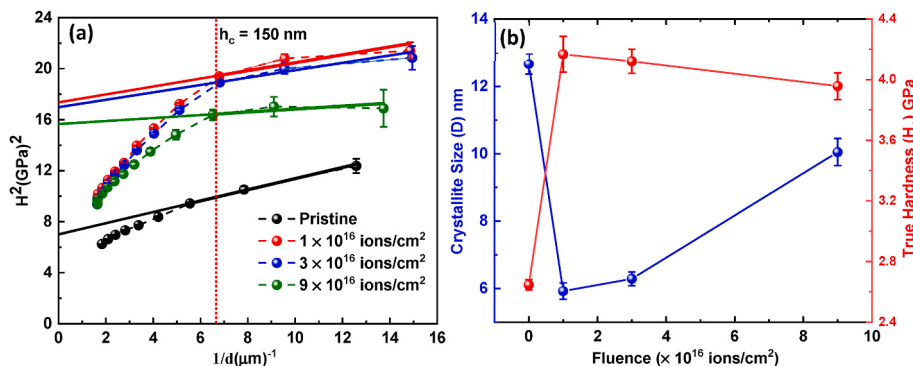


Fig. 8. (a) H^2 vs. $1/d$ plots, marked with the critical depth (h_c) and (b) variation of crystallite size and nanoindentation hardness with ion fluence for pristine and irradiated NiCoCrFePd HEA.

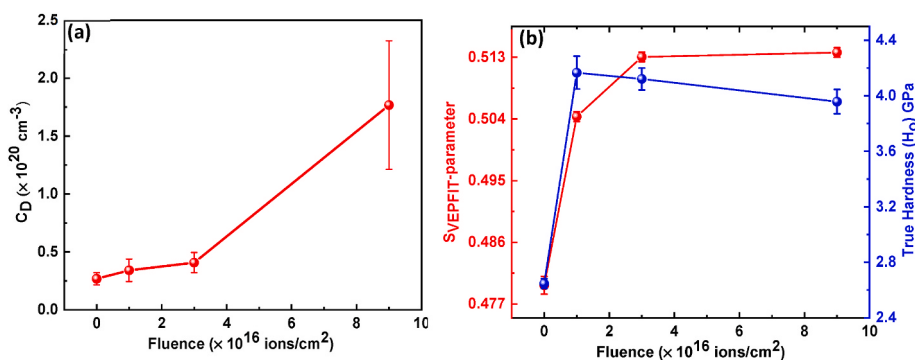


Fig. 9. (a) Vacancy concentration (C_D) variation with ion fluence evaluated using the positron diffusion length with the ion fluence, (b) S_{VEPFIT} -parameter along with the hardness in the damaged region i.e., true hardness (H_o) variations with the ion fluence.

Table 3

Variation in the hardness with ion fluence estimated from the fitting parameters of equation (2).

Ion fluence (ions/cm^2)	H_o (GPa)	h^* (nm)
Pristine	2.64 ± 0.03	62.392
1×10^{16}	4.16 ± 0.11	17.885
3×10^{16}	4.12 ± 0.07	17.048
9×10^{16}	3.95 ± 0.08	7.490

density at fluence $9 \times 10^{16} \text{ ions}/\text{cm}^2$ estimated from TEM was found $\sim 4.815 \times 10^{15} \text{ m}^{-2}$ comparable to that of the dislocation density of $\sim 9.92 \times 10^{15} \text{ m}^{-2}$ estimated from the XRD using the equations $\rho \sim 1/D^2$, where D is the crystallite size. It is important to note down here that similar results are also shown through molecular dynamics simulation with generation of mono vacancies till 0.3 dpa and an increase in the cluster size at higher fluence [23,50]. The formation of dislocation at higher fluence generally give rise to hardening because the dislocation serves as an obstacle for the atomic motions [51]. However, at the same time the irradiation-induced recrystallization, as evident from the increase in crystallite size from $5.92 \pm 0.24 \text{ nm}$ corresponding to $1 \times 10^{16} \text{ ions}/\text{cm}^2$ to $6.29 \pm 0.20 \text{ nm}$ at $3 \times 10^{16} \text{ ions}/\text{cm}^2$ and subsequently to $10.05 \pm 0.40 \text{ nm}$ at $9 \times 10^{16} \text{ ions}/\text{cm}^2$ leads to a decrease in the hardness at higher fluence. It is well-known that the irradiation-enhanced diffusion also accelerates the thermodynamically driven processes, thereby promoting dynamic recrystallization [52]. This indicates that the region of recrystallization would be free from any dislocations and thus, assist in reducing the hardness at higher ion fluences. A small suppression in the hardening behavior due to recrystallization at higher dose is also observed by Yan et al. [36]. The reduction in hardness to $4.12 \pm 0.07 \text{ GPa}$ and $3.95 \pm 0.08 \text{ GPa}$, corresponding to $3 \times 10^{16} \text{ ions}/\text{cm}^2$ and $9 \times 10^{16} \text{ ions}/\text{cm}^2$ respectively from $4.12 \pm 0.07 \text{ GPa}$ shows that recrystallization has the predominant effect in reducing the hardness of NiCoCrFePd HEA as compared to the dislocation induced hardening process. Thus, the collapsing of smaller size defects to large size dislocation defects has a lesser impact towards hardening compared to the softening due to improvement in the crystallinity because of recrystallization which give rise to the softening effect in NiCoCrFePd HEA corresponding to the ion fluence 3×10^{16} and $9 \times 10^{16} \text{ ions}/\text{cm}^2$, respectively.

5. Conclusions

We have experimentally observed the resistance against irradiation hardening behavior at high fluence under 1.05 MeV Xe^{+3} ion irradiation in the single-phase NiCoCrFePd HEA. Anomalous lattice contraction and fragmentation of crystallite size along with the generation of vacancies leads to irradiation-induced hardening at the initial ion fluence $1 \times 10^{16} \text{ ions}/\text{cm}^2$. Also, at the initial fluence the lattice contraction revealed

from the HR-TEM in conjuncture with the XRD investigations explains the irradiation induced stress relaxation in the lattice due to the inherent lattice distortion present in NiCoCrFePd HEA. With further increase in the ion fluence to $3 \times 10^{16} \text{ ions}/\text{cm}^2$ and $9 \times 10^{16} \text{ ions}/\text{cm}^2$, most of the small size point defects collapse to form large size dislocation, which ultimately increases the microstrain as well as crystallite size. Also, due to the strain produced, the defected region migrates towards the stress-free surface region with increase in the ion fluence as observed from the PADBS investigations. From the HR-TEM analysis, different size of dislocation loops ranging from (2 nm–6 nm) was observed with a dislocation density of $\sim 4.815 \times 10^{15} \text{ m}^{-2}$ corresponding to the sample irradiated with fluence $9 \times 10^{16} \text{ ions}/\text{cm}^2$ due to recombination of small defects. The effect of irradiation induced recrystallization on the retardation in the hardening process was found more dominant than the dislocation-induced hardening process. It is therefore concluded that owing to simultaneous recrystallization and recombination of point defects leads to the softening effect in the mechanical behavior at higher fluence, which is a good sign of resistance towards mechanical failure.

CRediT authorship contribution statement

Abid Hussain: Conceptualization, Methodology, Writing – original draft, Investigation, Interpretation, Formal analysis, Funding acquisition. **S.A. Khan:** Supervision, Resources, Writing – review & editing. **Sandeep K. Sharma:** Data curation, Formal analysis, Interpretation. **Kathi Sudarshan:** Data curation, Formal analysis, Interpretation. **Saurabh K. Sharma:** Formal analysis, Writing – review & editing. **Chetan Singh:** Data curation, Writing – review & editing. **P.K. Kulriya:** Supervision, Validation, Project administration, Writing – review & editing.

Declaration of competing interest

The authors declare that they have no known competing financial interests or personal relationships that could have appeared to influence the work reported in this paper.

Data availability

Data will be made available on request.

Acknowledgements

One of the authors A.H. is thankful to UGC for awarding Junior Research Fellowship with reference no.1330/(CSIR-UGC NET DEC. 2017). The author also acknowledges LEIBF at IUAC for a stable beam during the experiment, target preparations laboratory for the rolling machine, and providing the XRD facility. The author also acknowledges SPS and AIRF JNU for arc melting of HEA alloy samples preparation and

TEM characterization.

Appendix A. Supplementary data

Supplementary data to this article can be found online at <https://doi.org/10.1016/j.msea.2022.144523>.

References

- [1] W. Chen, X. Ding, Y. Feng, X. Liu, K. Liu, Z.P. Lu, D. Li, Y. Li, C.T. Liu, X.Q. Chen, Vacancy formation enthalpies of high-entropy FeCoCrNi alloy via first-principles calculations and possible implications to its superior radiation tolerance, *J. Mater. Sci. Technol.* 34 (2018) 355–364, <https://doi.org/10.1016/j.jmst.2017.11.005>.
- [2] Y. Zhang, T. Egami, W.J. Weber, Dissipation of radiation energy in concentrated solid-solution alloys: unique defect properties and microstructural evolution, *MRS Bull.* 44 (2019) 798–811, <https://doi.org/10.1557/mrs.2019.233>.
- [3] S. Shi, M. He, K. Jin, H. Bei, I.M. Robertson, Evolution of ion damage at 773K in Ni-containing concentrated solid-solution alloys, *J. Nucl. Mater.* 501 (2018) 132–142, <https://doi.org/10.1016/j.jnucmat.2018.01.015>.
- [4] Y. Lu, H. Huang, X. Gao, C. Ren, J. Gao, H. Zhang, S. Zheng, Q. Jin, Y. Zhao, C. Lu, T. Wang, T. Li, A promising new class of irradiation tolerant materials: Ti2ZrHfV0.5Mo0.2 high-entropy alloy, *J. Mater. Sci. Technol.* 35 (2019) 369–373, <https://doi.org/10.1016/j.jmst.2018.09.034>.
- [5] Q. Ding, Y. Zhang, X. Chen, X. Fu, D. Chen, S. Chen, L. Gu, F. Wei, H. Bei, Y. Gao, M. Wen, J. Li, Z. Zhang, T. Zhu, R.O. Ritchie, Q. Yu, Tuning element distribution, structure and properties by composition in high-entropy alloys, *Nature* 574 (2019) 223–227, <https://doi.org/10.1038/s41586-019-1617-1>.
- [6] F. Zhang, S. Lake, Y. Tong, O. Ridge, H. Bei, Z. University, W.J. Weber, Lattice distortion and phase stability of Pd-doped NiCoFeCr solid-solution alloys, *Entropy* 20 (2018) 900, <https://doi.org/10.3390/e20120900>.
- [7] Y. Tong, K. Jin, H. Bei, J.Y.P. Ko, D.C. Pagan, Y. Zhang, F.X. Zhang, Local lattice distortion in NiCoCr, FeCoNiCr and FeCoNiCrMn concentrated alloys investigated by synchrotron X-ray diffraction, *Mater. Des.* 155 (2018) 1–7, <https://doi.org/10.1016/j.matdes.2018.05.056>.
- [8] Y.F.W.Y. Kun Zhang, Y.L. Weiqi Tang, B. Wei, Evaluation of radiation response in CoCrFeCuNi high-entropy alloys, *Entropy* 20 (2018) 835, <https://doi.org/10.3390/e20110835>.
- [9] C. Lu, L. Niu, N. Chen, K. Jin, T. Yang, P. Xiu, Y. Zhang, F. Gao, H. Bei, S. Shi, M. R. He, I.M. Robertson, W.J. Weber, L. Wang, Enhancing radiation tolerance by controlling defect mobility and migration pathways in multicomponent single-phase alloys, *Nat. Commun.* 7 (2016) 1–8, <https://doi.org/10.1038/ncomms13564>.
- [10] Z. Zhang, D.E.J. Armstrong, P.S. Grant, The effects of irradiation on CrMnFeCoNi high-entropy alloy and its derivatives, *Prog. Mater. Sci.* 123 (2022), 100807, <https://doi.org/10.1016/j.jpmatsci.2021.100807>.
- [11] Y. Tong, G. Velisa, S. Zhao, W. Guo, T. Yang, K. Jin, C. Lu, H. Bei, D.C. Pagan, Y. Zhang, L. Wang, F.X. Zhang, Evolution of local lattice distortion under irradiation in medium- and high-entropy alloys, *Materialia* 2 (2018) 73–81, <https://doi.org/10.1016/j.jmsta.2018.06.008>.
- [12] Z. Wu, H. Bei, G.M. Pharr, E.P. George, Temperature dependence of the mechanical properties of equiatomic solid solution alloys with face-centered cubic crystal structures, *Acta Mater.* 81 (2014) 428–441, <https://doi.org/10.1016/j.actamat.2014.08.026>.
- [13] K. Jin, S. Mu, K. An, W.D. Porter, G.D. Samolyuk, G.M. Stocks, H. Bei, Thermophysical properties of Ni-containing single-phase concentrated solid solution alloys, *Mater. Des.* 117 (2017) 185–192, <https://doi.org/10.1016/j.matdes.2016.12.079>.
- [14] P. Bag, Y.C. Su, Y.K. Kuo, Y.C. Lai, S.K. Wu, Physical properties of face-centered cubic structured high-entropy alloys: effects of NiCo, NiFe, and NiCoFe alloying with Mn, Cr, and Pd, *Phys. Rev. Mater.* 5 (2021) 29–31, <https://doi.org/10.1103/PhysRevMaterials.5.085003>.
- [15] F. Granberg, K. Nordlund, M.W. Ullah, K. Jin, C. Lu, H. Bei, L.M. Wang, F. Djurabekova, W.J. Weber, Y. Zhang, Mechanism of radiation damage reduction in equiatomic multicomponent single phase alloys, *Phys. Rev. Lett.* 116 (2016) 1–8, <https://doi.org/10.1103/PhysRevLett.116.135504>.
- [16] C. Lu, T. Yang, K. Jin, G. Velisa, P. Xiu, M. Song, Q. Peng, F. Gao, Y. Zhang, H. Bei, W.J. Weber, L. Wang, Enhanced void swelling in NiCoFeCrPd high-entropy alloy by indentation-induced dislocations, *Mater. Res. Lett.* 6 (2018) 584–591, <https://doi.org/10.1080/21663831.2018.1504136>.
- [17] F. Tuomisto, K. Saarinen, D.C. Look, G.C. Farlow, Introduction and recovery of point defects in electron-irradiated ZnO, *Phys. Rev. B Condens. Matter* 72 (2005) 1–11, <https://doi.org/10.1103/PhysRevB.72.085206>.
- [18] P. Horodek, J. Dryzek, V.A. Skuratov, Studies of iron exposed to heavy ion implantation using positron annihilation spectroscopy, *Radiat. Phys. Chem.* 122 (2016) 60–65, <https://doi.org/10.1016/j.radphyschem.2016.01.031>.
- [19] S. Abbaya, R. Rajaraman, S. Kalavathi, C. David, B.K. Panigrahi, G. Amarendra, Effect of dose and post irradiation annealing in Ni implanted high entropy alloy FeCrCoNi using slow positron beam, *J. Alloys Compd.* 669 (2016) 117–122, <https://doi.org/10.1016/j.jallcom.2016.01.242>.
- [20] S. Abbaya, R. Rajaraman, C. David, Positron beam studies on the irradiation response of FeCrCoNi upon He ion implantation, *J. Alloys Compd.* 898 (2022), 162776, <https://doi.org/10.1016/j.jallcom.2021.162776>.
- [21] M. Elsayed, R. Krause-rehberg, C. Eisenschmidt, Defect study in CoCrFeMnNi high entropy alloy by positron annihilation lifetime spectroscopy, *Phys. Status Solidi* 215 (2018), 1800036, <https://doi.org/10.1002/pssa.201800036>.
- [22] L. Resch, M. Luckabauer, N. Helthuis, N.L. Okamoto, T. Ichitsubo, R. Enzinger, W. Sprengel, R. Würschum, Search for vacancies in concentrated solid-solution alloys with fcc crystal structure, *Phys. Rev. Mater.* 4 (2020), 60601, <https://doi.org/10.1103/PhysRevMaterials.4.060601>.
- [23] F. Tuomisto, I. Makkonen, J. Heikinheimo, F. Granberg, F. Djurabekova, *Acta Materialia Segregation of Ni at early stages of radiation damage in NiCoFeCr solid solution alloys*, *Acta Mater.* 196 (2020) 44–51, <https://doi.org/10.1016/j.actamat.2020.06.024>.
- [24] M.R. He, S. Wang, S. Shi, K. Jin, H. Bei, K. Yasuda, S. Matsumura, K. Higashida, I. M. Robertson, Mechanisms of radiation-induced segregation in CrFeCoNi-based single-phase concentrated solid solution alloys, *Acta Mater.* 126 (2017) 182–193, <https://doi.org/10.1016/j.actamat.2016.12.046>.
- [25] C. Lu, T. Yang, K. Jin, N. Gao, P. Xiu, Y. Zhang, F. Gao, H. Bei, W.J. Weber, K. Sun, Y. Dong, L. Wang, Radiation-induced segregation on defect clusters in single-phase concentrated solid-solution alloys, *Acta Mater.* 127 (2017) 98–107, <https://doi.org/10.1016/j.actamat.2017.01.019>.
- [26] T. ni Yang, C. Lu, G. Velisa, K. Jin, P. Xiu, Y. Zhang, H. Bei, L. Wang, Influence of irradiation temperature on void swelling in NiCoFeCrMn and NiCoFeCrPd, *Scripta Mater.* 158 (2019) 57–61, <https://doi.org/10.1016/j.scriptamat.2018.08.021>.
- [27] J.F. Ziegler, M.D. Ziegler, J.P. Biersack, SRIM - The stopping and range of ions in matter, 2010, *Nucl. Instrum. Methods Phys. Res. Sect. B Beam Interact. Mater. Atoms* 268 (2010) 1818–1823, <https://doi.org/10.1016/j.nimb.2010.02.091>.
- [28] R.E. Stoller, M.B. Toloczko, G.S. Was, A.G. Certain, S. Dwarkarnath, F.A. Garner, On the use of SRIM for computing radiation damage exposure, *Nucl. Instrum. Methods Phys. Res. Sect. B Beam Interact. Mater. Atoms* 310 (2013) 75–80, <https://doi.org/10.1016/j.nimb.2013.05.008>.
- [29] P. V Gaikwad, S.K. Sharma, S. Mukherjee, K. Sudarshan, A. Kshirsagar, Evolution of embedded lithium nanoclusters in lithium implanted alumina, *Mater. Chem. Phys.* 179 (2016) 143–151, <https://doi.org/10.1016/j.matchemphys.2016.04.086>.
- [30] A. van Veen, H. Schut, M. Clement, J.M.M. de Nijs, A. Kruseman, M.R. IJppma, VEPFIT applied to depth profiling problems, *Appl. Surf. Sci.* 85 (1995) 216–224, [https://doi.org/10.1016/0169-4332\(94\)00334-3](https://doi.org/10.1016/0169-4332(94)00334-3).
- [31] S.K. Sharma, V. Grover, R. Shukla, A. Hussain, A. Mishra, R.C. Meena, P.K. Kulriya, Evidence of improved tolerance to electronic excitation in nanostructured Nd₂Zr₂O₇, *J. Appl. Phys.* 129 (2021), 115902, <https://doi.org/10.1063/5.0039390>.
- [32] C.L. Dube, P.K. Kulriya, D. Dutta, P.K. Pujari, Y. Patil, M. Mehta, P. Patel, S. S. Khrirwadkar, Positron annihilation lifetime measurement and X-ray analysis on 120 MeV Au+7 irradiated polycrystalline tungsten, *J. Nucl. Mater.* 467 (2015) 406–412, <https://doi.org/10.1016/j.jnucmat.2015.05.029>.
- [33] K.C. Bhattacharya, B. Tripathi, N.K. Acharya, P.K. Kulriya, Y.K. Vijay, Formation of ZnTe by stacked elemental layer method, *Appl. Surf. Sci.* 255 (2008) 2143–2148, <https://doi.org/10.1016/j.apsusc.2008.07.068>.
- [34] R. Krause-Rehberg, H.S. Leipner, T. Abgarjan, A. Polity, Review of defect investigations by means of positron annihilation in II-VI compound semiconductors, *Appl. Phys. Mater. Sci. Process* 66 (1998) 599–614, <https://doi.org/10.1007/s00390050721>.
- [35] Q. Wan, G. Shu, R. Wang, H. Ding, X. Peng, Q. Zhang, J. Lei, Characterization of proton irradiation-induced defect in the A508-3 steel by slow positron beam, *Nucl. Instrum. Methods Phys. Res. B* 287 (2012) 148–152, <https://doi.org/10.1016/j.nimb.2012.04.013>.
- [36] C. Yan, R. Wang, X. Dai, Y. Wang, X. Wang, Investigation of hardening behavior in Xe ion-irradiated Zr e 1Nb, *J. Nucl. Mater.* 473 (2016) 256–263, <https://doi.org/10.1016/j.jnucmat.2016.03.003>.
- [37] R.S. Yu, M. Maekawa, A. Kawasuso, B.Y. Wang, L. Wei, Positron annihilation Doppler broadening study of Xe-implanted aluminum, *Appl. Surf. Sci.* 282 (2013) 724–728, <https://doi.org/10.1016/j.apsusc.2013.06.042>.
- [38] K.G. Lynn, D.M. Chen, R. Fork, S. Mycrs, Variable-energy positron-beam studies of Ni implanted with He, *Phys. Rev. B* 34 (1986) 1449–1458, <https://doi.org/10.1103/PhysRevB.34.1449>.
- [39] P. Hosemann, D. Frazer, M. Fratoni, A. Bolind, M.F. Ashby, Materials selection for nuclear applications: challenges and opportunities, *Scripta Mater.* 143 (2018) 181–187, <https://doi.org/10.1016/j.scriptamat.2017.04.027>.
- [40] G.M. Pharr, E.G. Herbert, Y. Gao, The indentation size effect : a critical examination of experimental observations and mechanistic interpretations, *Annu. Rev. Mater. Res.* 40 (2010) 271–292, <https://doi.org/10.1146/annurev-matsci-070909-104456>.
- [41] S. Jiang, L. Peng, H. Ge, Q. Huang, J. Xin, Z. Zhao, He and H irradiation effects on the nanoindentation hardness of CLAM steel, *J. Nucl. Mater.* 455 (2014) 335–338, <https://doi.org/10.1016/j.jnucmat.2014.06.053>.
- [42] Z. Zhu, H. Huang, J. Liu, J. Gao, Z. Zhu, Xenon ion irradiation induced hardening in inconel 617 containing experiment and numerical calculation, *J. Nucl. Mater.* 525 (2019) 32–39, <https://doi.org/10.1016/j.jnucmat.2019.07.032>.
- [43] M.D. McMurtrey, B. Cui, I. Robertson, D. Farkas, G.S. Was, Mechanism of dislocation channel-induced irradiation assisted stress corrosion crack initiation in austenitic stainless steel, *Curr. Opin. Solid State Mater. Sci.* 19 (2015) 305–314, <https://doi.org/10.1016/j.cossms.2015.04.001>.
- [44] X. Liu, R. Wang, A. Ren, J. Jiang, C. Xu, P. Huang, W. Qian, Y. Wu, C. Zhang, Evaluation of radiation hardening in ion-irradiated Fe based alloys by nanoindentation, *J. Nucl. Mater.* 444 (2014) 1–6, <https://doi.org/10.1016/j.jnucmat.2013.09.026>.
- [45] X. Zhang, X. Mei, Q. Zhang, X. Li, Y. Wang, Y. Wang, Study of irradiation damage induced by He²⁺ ion irradiation in Ni₆₂Ta₃₈ metallic glass and W metal, *Nucl.*

- Instrum. Methods Phys. Res. Sect. B Beam Interact. Mater. Atoms 406 (2017) 548–554, <https://doi.org/10.1016/j.nimb.2017.03.121>.
- [46] O.V. Boev, M.J. Puska, R.M. Nieminen, Electron and positron energy levels in solids, Phys. Rev. B 36 (1987) 7786–7794, <https://doi.org/10.1103/PhysRevB.36.7786>.
- [47] K. Siemek, P. Horodek, V.A. Skuratov, J. Waliszewski, A. Sohatsky, Positron annihilation studies of irradiation induced defects in nanostructured titanium, Vacuum 190 (2021), 110282, <https://doi.org/10.1016/j.vacuum.2021.110282>.
- [48] Y.P. Sharkeev, E.V. Kozlov, A.N. Didenko, S.N. Kolupaeva, N.A. Vihor, The mechanisms of the long-range effect in metals and alloys by ion implantation, Surf. Coating. Technol. 83 (1996) 15–21, [https://doi.org/10.1016/0257-8972\(95\)02777-7](https://doi.org/10.1016/0257-8972(95)02777-7).
- [49] J.E. Nathaniel, G.A. Vetterick, O. El-Atwani, A. Leff, J.K. Baldwin, P. Baldo, M. A. Kirk, K. Hattar, M.L. Taheri, The influence of solute on irradiation damage evolution in nanocrystalline thin-films, J. Nucl. Mater. 543 (2021), 152616, <https://doi.org/10.1016/j.jnucmat.2020.152616>.
- [50] C. Lu, K. Jin, L.K. Béland, F. Zhang, T. Yang, L. Qiao, Y. Zhang, H. Bei, H. M. Christen, R.E. Stoller, L. Wang, Direct observation of defect range and evolution in ion-irradiated single crystalline Ni and Ni binary alloys, Sci. Rep. 6 (2016) 1–10, <https://doi.org/10.1038/srep19994>.
- [51] O. Hall, Surface hardening IN ION-implanted metals, J. Nucl. Mater. 116 (1983) 123–126, [https://doi.org/10.1016/0022-3115\(83\)90300-8](https://doi.org/10.1016/0022-3115(83)90300-8).
- [52] J. Kim, J.W. Lim, J.K. Kim, D.H. Kim, E.S. Park, H.J. Chang, Suppressed radiation-induced dynamic recrystallization in CrFeCoNiCu high-entropy alloy, Scripta Mater. 190 (2021) 158–162, <https://doi.org/10.1016/j.scriptamat.2020.08.045>.